Journal of Nuclear Medicine, published on November 18, 2021 as doi:10.2967/jnumed.121.263145

Radioembolization Dosimetry with Total-Body ^{90}Y PET

Gustavo Costa[1], Benjamin Spencer[1], Negar Omidvari[1], Cameron Foster[2], Michael Rusnak[2], Heather Hunt[2], Denise T. Caudle[2], Rex T. Pillai[2], Catherine Tram Vu[2], Emilie Roncali[1,2]

Affiliations: Departments of [1]Biomedical Engineering and [2]Radiology, University of California-Davis, Davis, CA

Corresponding Author: Gustavo C A Costa,

Biomedical Engineering

UC Davis

One Shields Avenue

Davis, CA 95616

Email: gccosta@ucdavis.edu

Word count: 5,908

Financial Support: Funding for this work was provided by NIH grant R01 CA206187, which is supported by NCI, NIBIB and the Office of the Director, and by R01 CA249422.

Disclosure: No other potential conflicts of interest relevant to this article exist including employment, royalties, stock options, or patents.

Running title: ^{90}Y Total-Body PET TARE Dosimetry

ABSTRACT

Transarterial radioembolization (TARE) is a loco-regional radiopharmaceutical therapy based on the delivery of radioactive yttrium-90 (^{90}Y) microspheres to liver tumors. The importance of personalized dosimetry to make TARE safer and more effective has been demonstrated in recent clinical studies, stressing the need for quantification of the dose-response relationship to ultimately optimize the administered activity pre-treatment and image it post-treatment. ^{90}Y dosimetric studies are challenging due to the lack of accurate and precise methods but best realized with positron emission tomography combined with Monte Carlo simulations and other image modalities to calculate a segmental dose distribution. The aim of this study is to assess the suitability of imaging ^{90}Y PET patients with the total-body PET/CT uEXPLORER and to investigate possible improvements in TARE ^{90}Y PET-based dosimetry. The uEXPLORER is the first commercially available ultra-high-resolution (171 cps/kBq) total-body digital PET/CT with a 194 cm axial PET field of view that enables the whole body to be scanned in one bed position.

Methods: Two PET/CT scanners were evaluated in this study: the Biograph mCT and the total-body uEXPLORER. The reconstructions of a NEMA IQ phantom and two patient images were performed using our standard clinical oncology protocol. A late portal phase Contrast-Enhanced Computed Tomography was used to contour the liver segments and create corresponding volumes of interest. To calculate the absorbed dose, Monte Carlo simulations were carried out using Geant4 Application for Tomographic Emission (GATE). The absorbed dose and the dose volume histograms (DVH) were calculated for all six spheres (diameters ranging from 10 mm to 37 mm) of the NEMA phantom, the liver segments, and the entire liver. The differences between the phantom doses and an analytical ground truth were quantified through the root mean squared error.

Results: The uEXPLORER showed a higher signal to noise ratio at 10 mm and 13 mm diameter, consistent with its high spatial resolution and system sensitivity. The total liver absorbed dose showed excellent agreement between the uEXPLORER and the mCT for both patients, with differences lower than 0.2%. Larger differences of up to 60% were observed when comparing the liver segment doses. All DVHs were in good agreement, with narrower tails for the uEXPLORER in all segments, indicating a lower image noise.

Conclusions: This patient study is compelling for the use of total-body ^{90}Y PET for liver dosimetry. The uEXPLORER scanner showed a better signal-to-noise ratio than mCT especially in lower count regions of interest, which is expected to improve dose quantification and tumor dosimetry.

Key Words: Monte Carlo simulation, Radioembolization, yttrium-90, microspheres, radionuclide therapy, personalized medicine, dosimetry, liver cancer, quantitative imaging

INTRODUCTION

Transarterial radioembolization (TARE) is a loco-regional radionuclide therapy based on the delivery of radioactive yttrium-90 (^{90}Y) microspheres to liver tumors (1,2). TARE is increasingly integrated in multi-therapy approaches for both primary and metastatic liver cancer and has shown good potential to improve quality of life or downstage tumors for transplantation (3-6). It has also demonstrated a reduction in time-to-progression (6) with low toxicity (7,8) and has been adopted as the primary treatment for hepatocellular carcinoma at some institutions (3). The two commercially available ^{90}Y microspheres consisting of resin (SIR-Spheres, Sirtex) and glass (Theraspheres, Boston Scientific) are directly injected into the hepatic arteries through a catheter. The glass and resin microspheres have an average diameter of 20-60 μm and 20-30 μm and unit activity of 2500 Bq and 50 Bq, respectively, the latter requiring a larger amount of resin microspheres to achieve the same administered activity (9). The microspheres are mainly transported by the blood flow and tend to form clusters, thus presenting a very heterogeneous distribution in the liver. This can cause the absorbed dose to locally achieve values close to 400 Gy, much greater than the total liver target of 120 Gy and threatening sensitive hepatic structures (10-14). One major challenge in making TARE safer and more effective is the lack of accurate and precise methods to assess this heterogeneous dose distribution in the tumor and the rest of the liver post treatment. Because there is mounting evidence that TARE patient outcome correlates with the absorbed dose (15-19), it becomes critical to develop dosimetry methods that allow for quantitative evaluation of this relationship (e.g. progression-free survival vs. absorbed dose in Gy). Quantification of the dose-response relationship is required to optimize and understand the effects of administered activity and the potential need for re-treatment or treat adverse effects; 3D image-based dosimetry is a promising approach to achieve these goals (20).

Significant effort has been put on post-treatment monitoring, which is challenging due to the difficulty of imaging ^{90}Y, a beta emitter (99.98%) with a maximum energy of 2.28 MeV. Although ^{90}Y Bremsstrahlung X-ray photons are routinely imaged with a gamma camera or single photon emission computed tomography (SPECT), they form images with a very low signal-to-noise ratio and poor spatial resolution. This is due to the low photon emission yield per beta decay and the broad energy spectrum of these X-ray photons, preventing data correction and energy windowing (21). An alternative imaging modality for dosimetry is quantitative positron emission tomography (PET), possible through the limited ^{90}Y positron emission (0.0032% of decays). The spatial resolution of ^{90}Y PET is much better than ^{90}Y SPECT (21) but ^{90}Y PET dosimetry suffers from high bias and variability in small or low activity regions (22,23), preventing it from fully capturing the high heterogeneity of the liver dose distribution. The energy deposition at a voxel level (~3 mm) can nevertheless be easily computed with high accuracy through Monte Carlo simulations, such as the Geant4 Application for Tomographic Emission (GATE) toolkit. GATE is capable of modeling particle transport through matter and storing the energy deposited in a 3D map to compute voxel-based absorbed doses.

Recently, the advent of long axial field-of-view and total-body PET scanners have provided a substantial improvement in PET sensitivity over conventional PET scanners (24-26). The uEXPLORER scanner (Figure 1A) has an axial Field-Of-View (FOV) of 194 cm allowing the whole body to be scanned in one bed position and a large acceptance angle, which combined allow for a relatively flat sensitivity profile across 1 meter (figure 1B), providing a 16 to 64 fold gain in sensitivity for total-body imaging. For single organ imaging in the abdominal region positioned within the central meter, the sensitivity gain is expected to be 4 to 10 folds. This may

be especially beneficial for PET imaging of ^{90}Y which positron yield is 30,000 times lower than standard clinical oncology imaging with ^{18}F-FDG.

This work evaluated the suitability of imaging ^{90}Y PET patients with the total-body PET/CT uEXPLORER (United Imaging Healthcare) scanner installed at the University of California, Davis. It presents the very first use of the total-body PET for TARE dosimetry, and an investigation of the possible improvement in dose accuracy expected from the uEXPLORER sensitivity, 18 times higher than the conventional PET scanner used in this study according to the NEMA NU 2 standard, the Biograph mCT (Siemens Healthineers) (24,27). The images were used as input for Monte Carlo simulations to perform ^{90}Y liver radioembolization dosimetry and compare conventional and total-body clinical ^{90}Y PET/CT for the first time.

MATERIALS AND METHODS

System Parameters

The Biograph mCT (Siemens Healthineers) scanner is a PET/CT scanner with a FOV of 21.8 cm. The scanner has a sensitivity of 9.6 kcps/MBq; a spatial resolution of 4.5 mm at the center (21); and a Time-Of-Flight (TOF) resolution of 550 ps (27).

The uEXPLORER total-body PET/CT scanner (Figure 1) has an axial FOV of 194 cm, with a 57-degree axial acceptance angle. This leads to the highest sensitivity of any clinical PET scanner of 176 kcps/MBq as measured with the NEMA NU 2 protocol. The spatial resolution is 3.0 mm (28). The time-of-flight resolution was measured to be 505 ps following NEMA NU 2 2018.

Phantom Scan

A NEMA Image Quality (IQ) phantom was used to evaluate the image quality of both PET/CT scanners when imaging a therapeutic dose level of ^{90}Y (1-5 GBq) with the goal of calculating the absorbed dose. A Capintec CRC-55TR dose calibrator was used for ^{90}Y dose measurements after it was calibrated with a NIST traceable ^{90}Y source (Eckert & Ziegler GmbH) with an accuracy of +/- 3%. The phantom was filled with 2.51 GBq of ^{90}Y solution with a sphere-to-background ratio of 7.78:1 in the six fillable spheres (diameter 10-37 mm). The phantom was positioned with all spheres at the center of the axial FOV and imaged on day 0 for 30 minutes using a single bed position, first on the mCT then on the uEXPLORER to allow a direct comparison between the two scanners.

Patient Scans

A single-site, prospective study was approved by the Institutional Review Board to collect PET/CT images after ^{90}Y liver radioembolization. Two patients were imaged with PET/CT post radioembolization at UC Davis Health.

The first patient (P1) received a total activity of 3.363 GBq of ^{90}Y glass microspheres in three consecutive injections, targeting multiple neuroendocrine liver metastases. The patient was scanned 5 hrs after injection on the uEXPLORER total-body PET scanner (30-min duration) and then scanned on the mCT 1 hr later (30-min, 2-bed positions, 43% overlap). The second patient (P2) received a total activity of 0.985 GBq of ^{90}Y resin microspheres to treat metastatic pancreatic cancer. PET/CT images were acquired for 30 minutes with a single bed position covering the whole liver at 21.8 hrs and 22.6 hrs post-injection on the uEXPLORER and the mCT, respectively.

Image Reconstruction

Both phantom and patient data were reconstructed on the uEXPLORER using image reconstruction parameters adapted from the UC Davis clinical oncology protocol, but with an increased voxel size of 4 mm isotropic voxels opposed to 2.344 mm isotropic voxels: ordered subset expectation maximization (OSEM), 20 subsets, 4 iterations, TOF, point spread function (PSF) modeling, and no smoothing. This protocol follows the UC Davis low-dose image reconstruction parameters designed to reduce noise in low-count imaging such as for ^{90}Y imaging (29,30).

Image reconstruction on the mCT scanner used OSEM, TOF, 21 subsets, 3 iterations, PSF modeling, a voxel size of 4.078 x 4.078 x 3.75 mm^3, with a 5 mm Gaussian smoothing following the protocol specified by (31) and closely matched the clinical oncology protocol of this scanner except using a 5.0 mm Gaussian filter in order to reduce noise for low-count ^{90}Y imaging.

The voxel size of the uEXPLORER reconstructions provides the closest possible matched voxel size to the mCT reconstruction voxel size to reduce bias in the comparison. Given that the uEXPLORER has very high sensitivity and high spatial resolution, uEXPLORER images without smoothing are still less noisy than the mCT images (Figures 2A and 2B) and additional smoothing would likely over-smooth the images reducing diagnostic imaging performance .

Contrast-Enhanced Computed Tomography

Routine 4-phase abdominal Contrast-Enhanced Computed Tomography (CECT) images acquired pre-treatment were used for liver contouring and segmentation. The late portal phase image was used to identify the whole liver contour, vasculature, and define the eight Couinaud segments, S1 to S8 (including segments 4a and 4b) (32,33). A total of 13 volumes-of-interest

(VOIs) were created (Figures 2C and 2D), including the inferior vena cava (IVC), left and right portal veins (LPV and RPV). The absorbed dose depends largely on patients 1 and 2 liver masses (1504.8 g and 919.8 g, respectively) and the volumes and masses of all VOI can be seen in table 1. The segmentation was verified by a board-certified radiologist with nine years of experience.

^{90}Y Image-Based Dosimetry Using Monte Carlo Simulation

To calculate the absorbed dose from the activity distribution in the VOI, Monte Carlo simulations were carried out using GATE 9.0 (34). An attenuation map was generated for each patient or phantom using CECT and CT images, respectively, and material composition in GATE. The PET images were converted into activity distributions, then normalized to provide a probability density map of positron emission. The source and attenuation maps allowed GATE to generate and transport the primary and secondary particles (mostly electrons) and store the deposited energy in a 3D image matrix. The energy deposition matrix was weighted by its density to produce the final 3D absorbed dose distribution in Gy. The ^{90}Y physics was modeled through the standardem_opt4 package with a standard energy cut of 1 mm consistent with the liver tissue modeled in this work and as recommended for medical applications (35). The ^{90}Y radioactive decay energy distribution was defined by an energy spectrum generated from the Fermi theory for beta decays (36). ^{90}Y decays to ^{90}Zr through beta emission (99.998%) with a maximum energy of 2.28 MeV and mean energy of 930 keV, corresponding to a maximum electron range of 11 mm and a mean range of 2.5 mm in water (21). A low-frequency decay (0.017%) to the first excited state of ^{90}Zr allows the internal pair production transition to ground state, yielding on average 31.86 positron emission per million ^{90}Y decay that can be imaged with PET (37).

Phantom Absorbed Dose Calculation

The absorbed dose was estimated for each sphere insert of the NEMA IQ phantom. To prevent any voxel outside of the VOIs from containing a primary event in the Monte Carlo simulation and thus maximize the computation efficiency, a binary mask restricted the PET-based source distribution to voxels corresponding to each VOI. This allowed the simulations to be carried out with a fixed number of primary events followed by scaling to the cumulative activity instead of using the true total number of events, typically very large with therapeutic activities of 1-5 GBq. A total of 10^7 primaries was chosen that provided a statistical uncertainty of approximately 1% for the 37 mm sphere with a reasonable simulation time of 2 hours in a 8-core computer at 3.2 GHz and 64 GB of RAM. The resolution of the volumetric dose map generated by GATE was 4 mm isotropic and 4.07 x 4.07 x 3.75 mm^3 for the uEXPLORER and the mCT, respectively. A separate Monte Carlo simulation was performed to produce the ground truth dose map through a mathematical model of the IQ phantom. The ground truth was calculated with MC simulation exactly as for the image-based calculations, but using geometrical spheres, an homogeneous radiation source and 0.25 x 0.25 x 0.25 mm^3 voxels to allow accurate tracking of beta particles with ranges up to 11 mm. To compensate for the small voxel size, a total of 10^8 primaries per sphere was used to achieve a statistical uncertainty of approximately 5% for the 37 mm sphere.

Patient Absorbed Dose Calculation

The noise in ^{90}Y-PET images is inherently higher than in ^{18}F images due to the low positron yield combined with a lack of specific reconstructions methods to address the low count statistics

(37). This limitation poses a unique challenge to define the liver volume directly on the PET image especially in the presence of respiratory motion shifting the liver position (38). Segmenting different images separately (e.g. mCT and uEXPLORER) also adds bias on the absorbed dose distributions, which was mitigated by using a single VOI generated from the contoured CECT. The PET images were co-registered to the CECT then projected onto the CECT image grid. Since PET images are used as radiation sources, every count in the image is a probable location of a primary event. To ensure all primary events were generated only in the liver, the same technique used with the phantom was applied in which the liver VOI was used as a binary image mask to restrict primary event generation to regions within the liver (Figure 3).

Monte Carlo simulations were carried out within a voxelized phantom created from the CECT image that provided the anatomical information, mass, and density of tissue in which the beta particles propagate and interact. The activity distribution measured from PET images registered to the CECT volume was used to define the ^{90}Y source with 10^8 primary events, with a voxel size matching the spatial resolution of the CECT images (0.74 x 0.74 x 1.25 mm^3 and 0.67 x 0.67 x1.00 mm^3, for patient 1 and 2 respectively). All voxel-based absorbed doses were calculated from the dose map by averaging the voxel values in the VOI using that all voxels share the same mass and density. No ground-truth was computed, as no *in vivo* quantification of the ^{90}Y microspheres distribution can be performed to confirm the ^{90}Y activity distribution measured with PET.

Dose Characterization

The absorbed dose and dose volume histograms (DVH) were calculated for each phantom sphere, each liver segment, and the entire liver from the 3D absorbed dose distributions. DVHs

for individual segments and the whole liver were used to assess the difference in the dose distributions computed from each PET/CT scanner. A particular range of dose bins was also evaluated where it considers only the voxels between 20% and 80% of the maximum absorbed dose (Gy) to build the cumulative DVH ($DVH_{20\%-80\%}$). This approach avoids errors near extrema where the noise might be increased and make the the data trends clearer (37).

With the NEMA spheres, where ground-truth was available, the difference between the true value and those obtained with the scans was also quantified through the Root Mean Squared Error (RMSE) (39):

$$\mathrm{RMSE}=\frac{\sqrt{\sum_{0}^{100}\left(\mathrm{DVH}_{\mathrm{PET},ø}-\mathrm{DVH}_{\mathrm{True},ø}\right)^{2}}}{100}$$

where $DVH_{PET,ø}$ is the image-based absorbed dose, and $DVH_{True,ø}$ is the true absorbed dose from the ground truth. The RMSE was calculated for the whole volume as well as for the 20-80% ($RMSE_{20\%-80\%}$) range.

RESULTS

Phantom Analysis

Figure 4A shows the dose differences between the ground truth, the mCT and uEXPLORER for all six spheres. The mCT scanner at 10 mm and 13 mm diameter showed negative biases of 14.4 Gy and 14.5 Gy, respectively. The uEXPLORER showed differences of 7.9 Gy and 1.4 Gy for these volumes, respectively. The lower biases were consistent with the higher sensitivity and spatial resolution of the uEXPLORER, expected to improve the dosimetry accuracy primarily in low count ^{90}Y-PET regions resulting from small or low activity regions.

Figure 4B shows the $DVH_{20\%-80\%}$ of the 37 mm sphere for both the uEXPLORER and mCT scanners as well as for the ground truth. The ^{90}Y beta particles may deposit their energy in a neighbor voxel or even outside the sphere leading to a heterogeneous energy deposition and, therefore, the $DVH_{20\%-80\%}$ exhibits a slow decrease rather than being a step function. The 37 mm sphere accounts for a larger number of voxels and thus resulted in a good RMSE agreement with the ground truth for both PET scanners, with no significant difference (0.3%) between the scanners RMSE. Although the RMSE was lower for the uEXPLORER in four out of six spheres, including the two smallest spheres of 10 mm and 13 mm diameter, it varied largely with no clear trend between the two scanners. The $RMSE_{20\%-80\%}$ did not further improve the analysis, with a 36%-140% variation from the ground truth.

Patient Dosimetry

The total liver absorbed dose calculated from the PET distribution showed excellent agreement between the uEXPLORER and the mCT, with 108 Gy (difference of 0.2 Gy - 0.19%) for patient 1 and 40 Gy (difference of 0.1 Gy - 0.16%) for patient 2. Much larger differences were observed when comparing the dose in liver segments ranging from 6 Gy to 204 Gy (differences from 0.01% to 60.8%) for P1 (Figure 5A) and 10 Gy to 92 Gy (differences from 0.39% to 35.8%) for P2 (Figure 5B) .

Figure 6 shows the $DVH_{20\%-80\%}$ for segments 6, 7, and 8 in both patients 1 and 2. These segments had the highest activities and absorbed doses, thus also better count statistics and lower noise that provide the most robust comparison between the two scanners. All $DVH_{20\%-80\%}$ were in good agreement, with narrower tails for the uEXPLORER in all segments. As reported by (39), a narrower tail might be an indicator of lower image noise. This was clearer in P2, who

received a lower injected activity and was imaged at a later time point than P1 (5 h and 22 h post-injection, respectively) and therefore should have a lower signal-to-noise ratio. Accordingly, the lower image noise of the uEXPLORER agreed with the improved average contrast recovery reported by (28).

DISCUSSION

The absorbed doses calculated for the NEMA phantom spheres imaged with uEXPLORER and mCT scanners agreed well for most of the four largest spheres with an expected fluctuation due to the inherent noise present in ^{90}Y-PET images. In contrast, a larger discrepancy with the ground truth of 1.0% and 10.2% was observed for the 13 mm diameter sphere with the uEXPLORER and the mCT, respectively. This is a clear indication of the higher spatial resolution and signal-to-noise ratio of the uEXPLORER which is especially beneficial for dose quantification in small and low activity regions. This trend is also observed in patient images where the narrower tail of the uEXPLORER $DVH_{20\%-80\%}$ indicates a lower noise level, more apparent for P2 who received a lower injected activity and was scanned at a later time point, resulting in a two-fold reduction of counts.

The $DVH_{20\%-80\%}$ for both the phantom and the patients show a very similar slope in both scanners and the behavior of the slope indicates the heterogeneity of the dose or, in this case, the activity source. In a homogeneous source all voxels have the same value and, therefore, the $DVH_{20\%-80\%}$ would be a step function. In a heterogeneous source, the voxels have different values resulting in slopes like those shown in figures 4B and 6. Hence, the similarities in the DVH slope for both scanners suggest a similar distribution of activity. Similar distributions and

heterogeneities obtained from the two subsequent PET scans suggest that ^{90}Y PET can be considered as a reliable method for post-treatment dosimetry and follow-up.

P1 received three selective injections through the right hepatic artery targeting three main arterial branches supplying multiple tumors in the right hepatic lobe, resulting in high doses in target segments S5 to S8. Segments S1-S4 and the vessels should contain no or very little activity due to the injection location, meaning that the observed dose is likely due to inaccuracies in PET corrections during reconstruction (e.g. scatter and dead-time correction and LYSO background subtraction). P2 received a single lobar injection in the right hepatic artery prior to lobectomy, resulting in a more uniform absorbed dose distribution in segments S5 to S8 than P1 due to a more widespread microsphere distribution. Most of the resin microspheres were directed to the right lobe but a substantial amount of activity reached the left lobe, possibly due to the large number of microspheres leading to a reflux into unintended artery branches (9), explaining the high doses on segments 4a and 4b and stressing the need for post-treatment dosimetry. Although P2 was injected with much lower activity than P1 (25%), the absorbed dose for the entire liver volume was 35% of P1's liver dose, due to the much smaller liver mass (919.8 g and 1504.8 g, respectively). The low VOIs masses (2 g to 26 g derived from organ volumes), such as the vessels, can cause even a very low ^{90}Y activity to generate a high absorbed dose with a high degree of uncertainty. This also explains why the absorbed dose in S5 and S7 is greater for P2 than P1 despite the lower injected activity. The intra-liver discrepancies and the changes in absolute dose values indicate the importance of conducting a segmental dose assessment for ^{90}Y radioembolization instead of evaluating the whole liver dose that includes the total mass even if not irradiated and decreases the mean absorbed dose. Furthermore, recent studies showed lobules trapping 1 to 453 microspheres resulting in a highly nonuniform distribution (14), creating high

doses locally and, therefore, it is critical to measure the dose heterogeneity and move towards high-resolution dosimetry.

CONCLUSION

Personalized dosimetry is of great interest in TARE and a detailed evaluation of the absorbed dose in the liver through Couinaud's liver segments allows a better understanding of the distribution of the microspheres and evaluation of the treatment. The whole liver absorbed doses calculated from two different PET scans were in high agreement with each other indicating both conventional and total body PET provide good ^{90}Y dosimetry. This agreement builds up the confidence on using ^{90}Y PET over bremsstrahlung SPECT with the possibility of assessing the microsphere placement and dosimetry post-treatment.

Performing segmental liver dosimetry not only can indicate the dose-response of the treatment but can help improve patient care. Understanding the activity may either confirm the planning or elucidate an unexpected distribution and might support the increase of the injected activity when low toxicity is confirmed.

The uEXPLORER provides a more detailed activity and absorbed dose distribution, translating into a more accurate visualization and quantification of microspheres clusters. This is particularly important when analyzing the liver segments or small volumes and tumors. Although the EXPLORER image is visibly clearer, only the relative difference with conventional PET can be computed, since there is no in-vivo ground truth to confirm the microsphere distributions.

The better accuracy observed in the small spheres of the NEMA phantom and the greater spatial resolution of uEXPLORER made the co-registration between the PET and the CT images

faster and more accurate, indicating the potential of total-body PET for intra-liver dosimetry. This will be investigated in further patient studies.

ACKNOWLEDGEMENTS

Funding for this work was provided by NIH grant R01 CA206187, which is supported by NCI, NIBIB and the Office of the Director, and by R01 CA249422.

KEY POINTS

QUESTION: What is the impact of evaluating TARE dose distribution at the liver segment scale and what is the advantage of using high-sensitivity total-body PET?

PERTINENT FINDINGS: Segmental calculation of the absorbed dose resulted in large discrepancies between the total-body and conventional PET scanners while the evaluation of the entire liver exhibits good agreement and the uEXPLORER shows better signal-to-noise ratio in both phantom and patient evaluations.

IMPLICATIONS FOR PATIENT CARE: The use of PET images opens the possibility of post-treatment follow up and dosimetry with the calculation of the absorbed dose by Couinaud's liver segments which helps evaluating the treatment with the detailed separation of irradiated and non-irradiated volumes.

REFERENCES

1. Sirtex website. http://www.sirtex.com/us/clinicians/about-sir-spheres-microspheres/. Accessed July 20th 2021.
2. Sirtex technology pty ltd: Pilot study of Selective Internal Radiation Therapy (SIRT) with yttrium-90 resin microspheres (SIR-Spheres microspheres) in patients with Renal cell carcinoma (STX0110). | RESIRT. Trial id ACTRN12610000690055. Autralian cancer trials website. Http://australiancancertrials.Gov.Au. Accessed July 20th 2021.
3. Salem R, Gabr A, Riaz A, et al. Institutional decision to adopt Y90 as primary treatment for hepatocellular carcinoma informed by a 1,000-patient 15-year experience. *Hepatology*. 2018;68:1429-1440.
4. Garin E, Rolland Y, Edeline J. 90Y-loaded microsphere SIRT of HCC patients with portal vein thrombosis: high clinical impact of 99mTc-MAA SPECT/CT-based dosimetry. *Semin Nucl Med*. 2019;49:218-226
5. Salem R, Johnson G E, Kim E, et al. Yttrium-90 radioembolization for the treatment of solitary, unresectable HCC: the legacy study. *Hepatology*. 2021. Epub ahead of print.
6. Salem R, Gordon A C, Mouli S, et al. Y90 radioembolization significantly prolongs time to progression compared with chemoembolization in patients with hepatocellular carcinoma. *Gastroenterology*. 2016;151:1155-1163.
7. Padia S A, Johnson G E, Horton K J, et al. *S*egmental yttrium-90 radioembolization versus segmental chemoembolization for localized hepatocellular carcinoma: results of a single-center, retrospective, propensity score-matched study. *J Vasc Interv Radiol*. 2017;28:777-785.
8. Chow P K H, Gandhi M, Tan S B, et al. Asia-pacific hepatocellular carcinoma trials group. SIRveNIB: selective internal radiation therapy versus Sorafenib in asia-pacific patients with hepatocellular carcinoma. *J Clin Oncol*. 2018;36:1913-1921.
9. Kallini J R, Gabr A, Thorlund K, et al. Comparison of the adverse event profile of TheraSphere® with SIR-Spheres® for the treatment of unresectable hepatocellular carcinoma: a systematic review. *Cardiovasc Intervent Radiol*. 2017;40:1033-1043.

10. Cheneler D, Ward M. Power output and efficiency of beta-emitting microspheres. *Radiat Phys Chem*. 2015;106:204-212.
11. Dewaraja Y K, Schipper M J, Shen J, et al. Tumor-absorbed dose predicts progression-free survival following (131)I-Tositumomab radioimmunotherapy. *J Nucl Med*. 2014;55:1047-53.
12. Elschot M, Lam M G E H , van den Bosch M A A J, Viergever M A , de Jong H W A M. Quantitative monte carlo–based 90Y SPECT reconstruction. *J. Nucl. Med.* 2013;54:1557-1563.
13. Elschot M, Vermolen B J, Lam M G, de Keizer B, van den Bosch MA, de Jong H W. Quantitative comparison of PET and bremsstrahlung SPECT for imaging the in vivo yttrium-90 microsphere distribution after liver radioembolization. *PLoS One* 2013;8.
14. Walrand S. Microsphere deposition, dosimetry, radiobiology at the cell-scale, and predicted hepatic toxicity. In: Handbook of radioembolization. *Taylor & Francis*; 2016:199-217
15. Garin E, Lenoir L, Rolland Y, et al. Dosimetry based on 99mTc-macroaggregated albumin SPECT/CT accurately predicts tumor response and survival in hepatocellular carcinoma patients treated with 90Y-loaded glass microspheres: preliminary results. *J Nucl Med*. 2012;53:255-63
16. Fabbri C, Sarti G, Cremonesi M, et al. Quantitative analysis of 90Y bremsstrahlung SPECT-CT images for application to 3D patient-specific dosimetry. *Cancer Biother. Radiopharm*. 2009;24:145-154.
17. Fong Y, Kemeny N, Paty P, Blumgart L H, Cohen A M. Treatment of colorectal cancer: hepatic metastasis. *Seminars in Surgical Oncology.* 1996;12:219-252.
18. Fowler K J, Maughan N M , Laforest R, et al. PET/MRI of hepatic 90Y microsphere deposition determines individual tumor response. *Cardiovasc Intervent Radiol.* 2016;39:855-864.
19. Garin E, Palard X, Rolland Y. Personalised dosimetry in radioembolisation for HCC: impact on clinical outcome and on trial design. *Cancers (Basel)*. 2020;12:1557.
20. Ljungberg M, Gleisner K S. Three-dimensional image-based dosimetry in radionuclide therapy. *IEEE Trans. Rad. Pla. Med. Sci*. 2018 :1-1.

21. O'Doherty J. A review of 3D image-based dosimetry, technical considerations and emerging perspectives in 90Y microsphere therapy. *Journal of Diagnostic Imaging in Therapy.* 2015;2:1-34.
22. Tang S, Liu Y, Wang J, Zhao Y, Fan X, Dong Y. Dead time correction method for long axial field-of-view, whole-body PET scanner. *J Nucl Med*. 2019;60:458.
23. Tang S, Zhao Y, Wang J, Liu Y, Dong Y. Geometric correction in normalization for long axial field-of-view, whole-body PET scanner. *IEEE Nuclear Science Symposium and Medical Imaging Conference (NSS/MIC)*. 2019.
24. Spencer B A, Berg E, Schmall J P, et al. Performance evaluation of the uEXPLORER Total-body PET/CT scanner based on NEMA NU 2-2018 with additional tests to characterize long axial field-of-view PET scanners. *J Nucl Med*. 2021;62:861-870.
25. Karp J S, Viswanath V, Geagan M J, et al. PennPET Explorer: design and preliminary performance of a whole-body imager. *J Nucl Med*. 2020;61:136-143.
26. Prenosil G A, Sari H, Fürstner M, et al. Performance characteristics of the Biograph Vision Quadra PET/CT system with long axial field of view using the NEMA NU 2-2018 Standard. *J Nucl Med*. 2021;Epub ahead of print.
27. Jakoby B W, Bercier Y, Conti M, Casey M E, Bendriem B, Townsend D W. Physical and clinical performance of the mCT time-of-flight PET/CT scanner. *Phys Med Biol*. 2011;56:2375–2389.
28. Spencer B, Omidvari N, Costa G, et al. Comparison between EXPLORER total-body PET with conventional PET imaging of Y-90 radioembolization: a phantom and clinical study. IEEE-MIC 2020
29. Badawi R D, Shi H, Hu P, et al. First human imaging studies with the EXPLORER total-body PET scanner. *J Nucl Med*. 2019;60:299-303
30. Leung E K, Berg E, Omidvari N et al. Quantitative accuracy in total-body imaging using the uEXPLORER PET/CT scanner. *Phys Med Biol.* 2021. Epub ahead of print. .
31. Willowson K P, Hayes A R, Chan D L H, et al.. Clinical and imaging-based prognostic factors in radioembolisation of liver metastases from colorectal cancer: a retrospective exploratory analysis. *EJNMMI*. 2017;7:46.

32. Majno P, Mentha G, Toso C, Morel P, Peitgen H O, Fasel J H. Anatomy of the liver: an outline with three levels of complexity--a further step towards tailored territorial liver resections. J *Hepatol*. 2014;60:654-62.
33. Bismuth H, Houssin D, Castaing D. Major and minor segmentectomies “réglées” in liver surgery. *World J. Surg.* 1982;6**:**10–24.
34. Sarrut D, Bardiès M, Boussion N, et al. A review of the use and potential of the GATE Monte Carlo simulation code for radiation therapy and dosimetry applications. *Med. Phys.* 2014;41:064301.
35. Beaudoux V, Blin G, Barbrel B, Kantor G, Zacharatou C. Geant4 physics list comparison for the simulation of phase-contrast mammography (XPulse project). P*hysica Medica. 2019;*60:66–75
36. Roncali E, Taebi A, Foster C, Vu C T. Personalized dosimetry for liver cancer Y-90 radioembolization using computational fluid dynamics and monte carlo simulation. *Ann Biomed Eng*. 2020;48:1499-1510.
37. Strydhorst J, Carlier T, Dieudonné A, Conti M, Buvat I. A GATE evaluation of the sources of error in quantitative 90Y PET. *Med Phys*. 2016;43:5320.
38. Tsai Y L, Wu C J, Shaw S, Yu P C, Nien H H, Lui L T. Quantitative analysis of respiration-induced motion of each liver segment with helical computed tomography and 4-dimensional computed tomography. *Radiat Oncol.* 2018;13:59
39. Siman W, Mikell J K, Mawlawi O R, Mourtada F, Kappadath S C. Dose volume histogram-based optimization of image reconstruction parameters for quantitative 90Y-PET imaging. *Med Phys*. 2019;46:229-237.

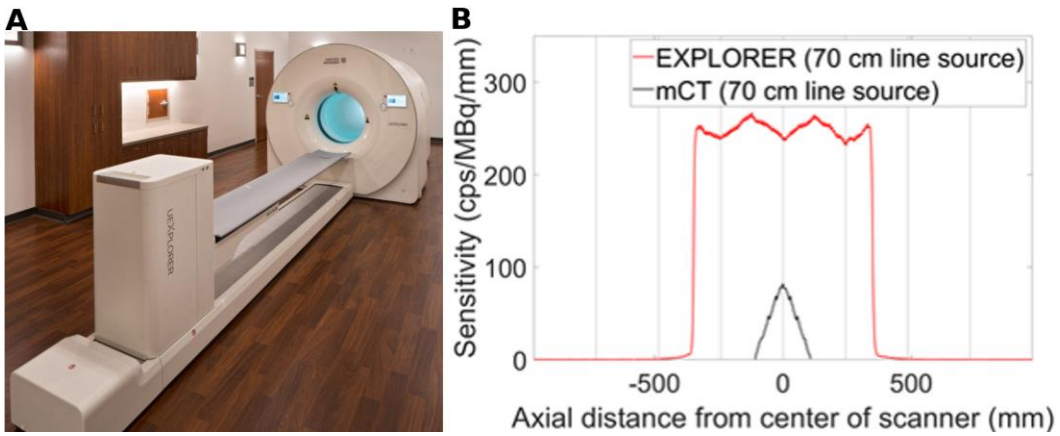

FIGURE 1. (A) Photograph of the uEXPLORER total-body PET/CT scanner installed at the EXPLORER Molecular Imaging Center in Sacramento, CA, USA. (B) Comparison of sensitivity profiles between the mCT and uEXPLORER.

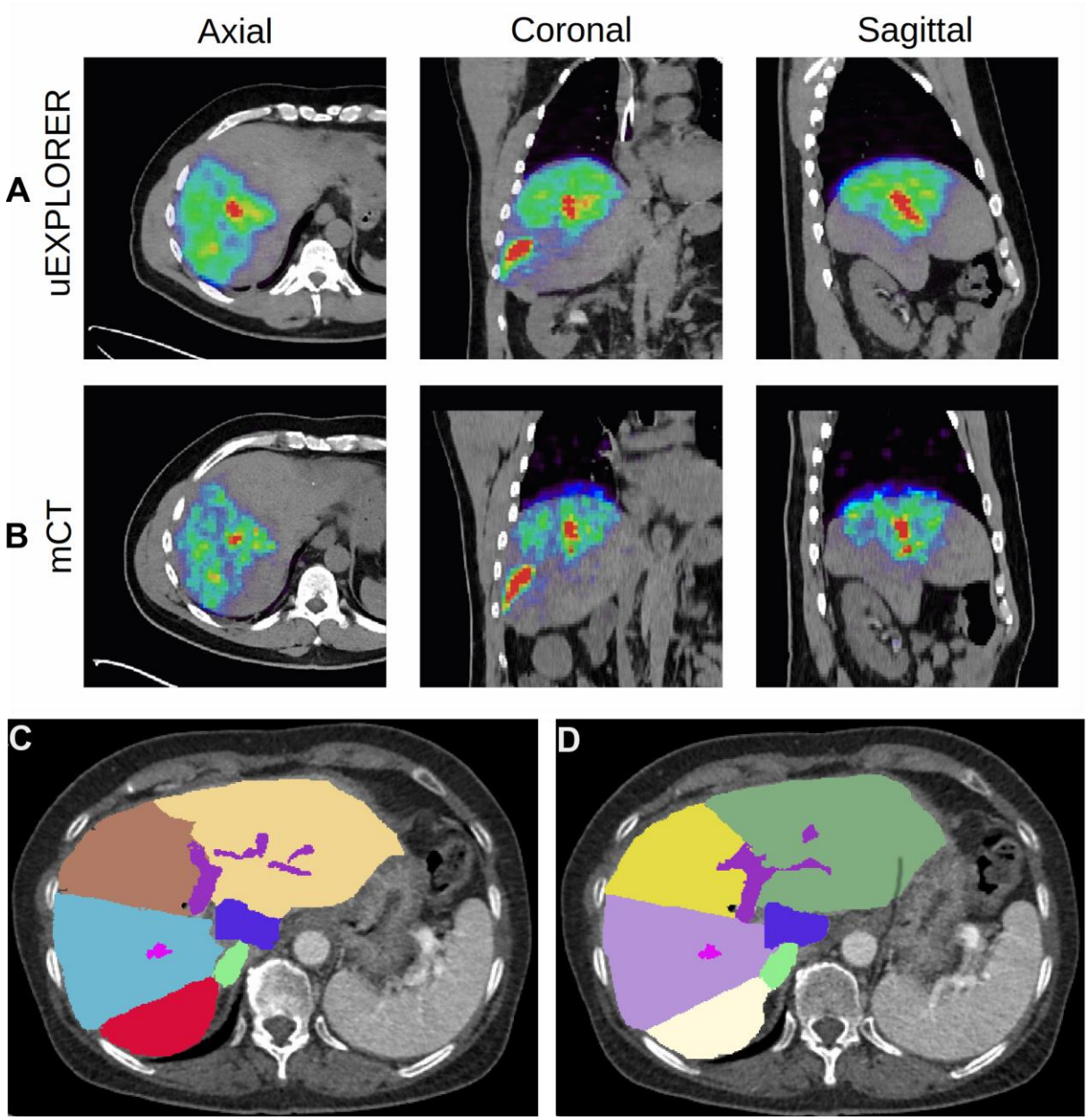

FIGURE 2. Patient images of PET/CT at axial, coronal and sagittal views from the (A) uEXPLORER and (B) mCT. The uEXPLORER images without smoothing are less noisy than the mCT and additional smoothing to the uEXPLORER. And the CECT at axial view with Couinaud segments at the (C) upper liver containing segments 2, 4a, 7 and 8 and (D) bottom liver containing segments 3, 4b, 5 and 6. IVC, LPV and RPV can be visualized in both upper and bottom liver.

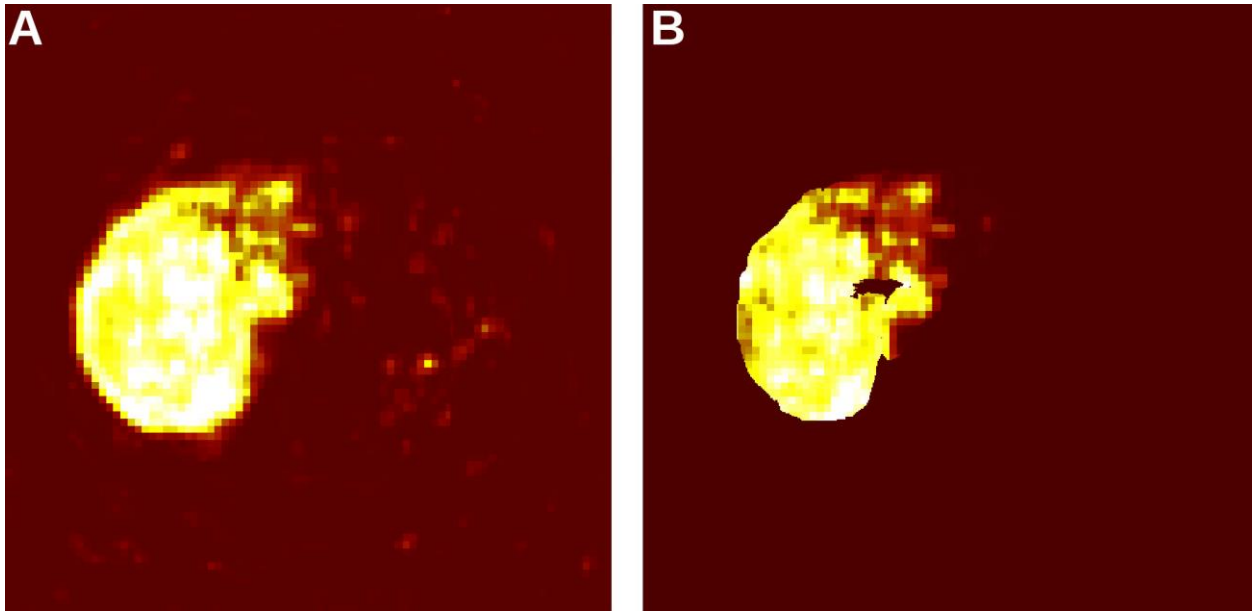

FIGURE 3. (A) Patient 2 activity distribution with 957 MBq in the entire mCT PET image and (B) after applying a mask corresponding to the VOI to limit the generation of events to the VOI.

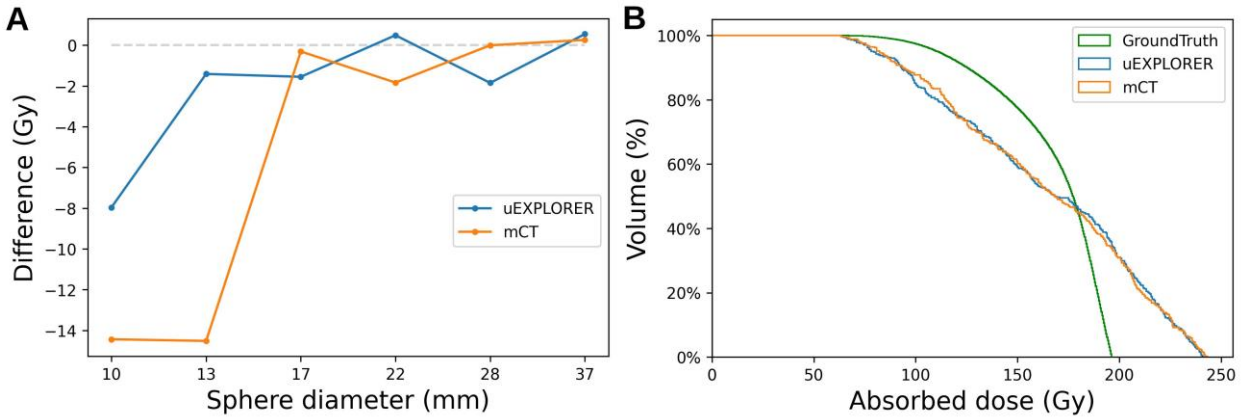

FIGURE 4. (A) Absolute differences between the uEXPLORER and mCT versus the true absorbed doses from the ground truth for the six NEMA spheres and (B) dose volume histogram of the 37 mm sphere with 20% to 80% range of the maximum absorbed dose (Gy).

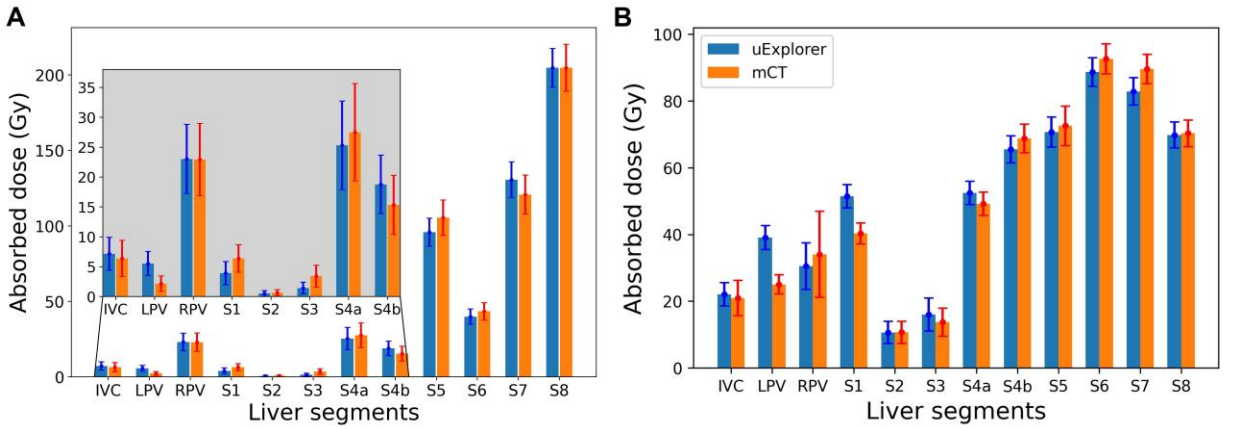

FIGURE 5. Absorbed doses for (A) patient 1 and (B) patient 2 . Error bars indicate the statistical uncertainty from GATE simulations.

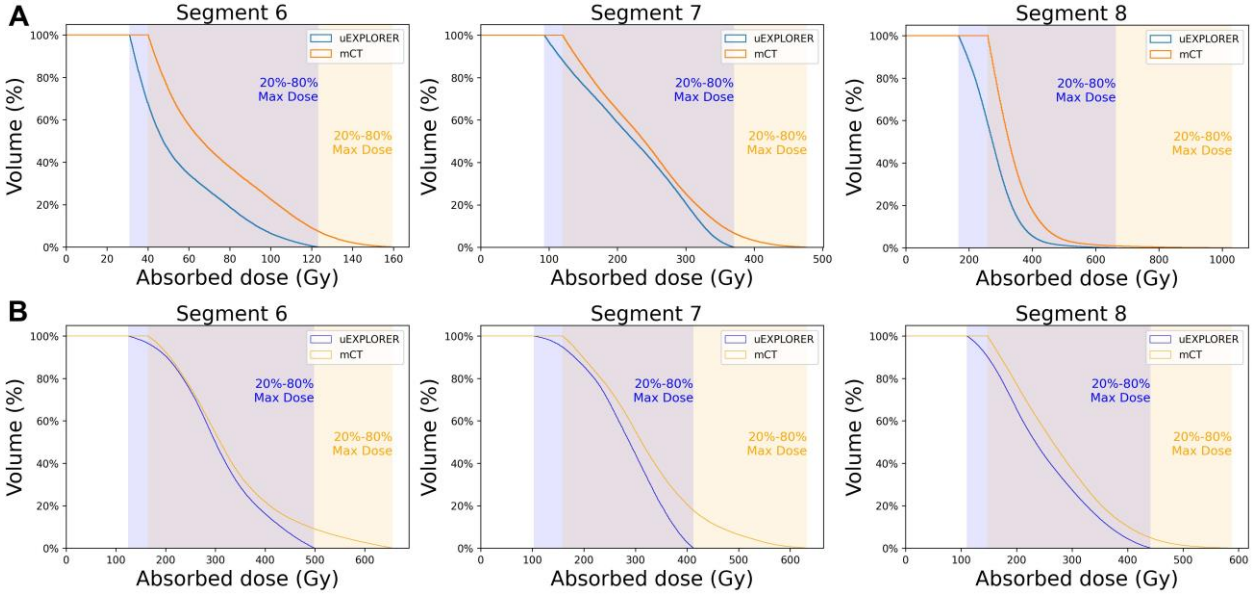

FIGURE 6. Dose volume histogram with 20%-80% range of the maximum absorbed dose (Gy) for segments 6, 7 and 8 of (A) patient 1 and (B) patient 2.

TABLE 1. Patients 1 and 2 liver and liver segments volumes and masses.

		Liver	**IVC**	**LPV**	**RPV**	**S1**	**S2**	**S3**	**S4a**	**S4b**	**S5**	**S6**	**S7**	**S8**
P 1	**Volume(ml)**	1417.5	22.23	2.56	24.39	24.52	129.9	45.94	199.73	36.9	186.48	49.19	212.57	483.09
	Mass (g)	1504.8	23.6	2.72	25.89	26.03	137.9	48.77	212.03	39.17	197.97	52.22	225.66	512.85
P 2	**Volume(ml)**	866.5	33.96	6.61	9.6	14.04	91.46	155.39	124.9	87.93	169.27	34.0	22.66	116.67
	Mass (g)	919.8	36.05	7.02	10.19	14.9	97.09	164.96	132.59	93.35	179.7	36.09	24.06	123.86

Graphical Abstract